# *Ab initio* study of boron in α-iron: Migration barriers and interaction with point defects

A. F. Bialon, T. Hammerschmidt, and R. Drautz
*Atomistic Modelling and Simulation, ICAMS, Ruhr-Universität Bochum, D-44801 Bochum, Germany*
(Received 11 December 2012; published 20 March 2013)

Boron is a common alloying element in modern steels with a significant influence on the mechanical properties already at concentrations of only a few parts per million. The effect of boron depends on its distribution in the microstructure. Here, we characterize the elemental factors that determine the boron distribution in α-iron by density functional theory calculations. Boron as point defect has been considered in substitutional and interstitial sites. The calculated migration barriers for the substitutional and interstitial mechanisms show the first nearest-neighbor hops being preferred over second nearest-neighbor hops. A dissociative mechanism shows boron migrating via an interstitial mechanism to be likely trapped by vacancies. In order to characterize the interaction with other point defects, we determined the distance-dependent interaction energy of a boron defect with a vacancy, a second boron, and with hydrogen, carbon, nitrogen, oxygen, aluminum, silicon, phosphorus, and sulfur atoms. We find that substitutional boron binds strongly to interstitial point defects with dumbbell formation and weaker to substitutional point defects. Interstitial boron tends to repel substitutional and interstitial point defects. We find a similarity of substitutional boron and vacancies regarding their influence on elastic properties and their interaction with point defects in α-iron.

DOI: 10.1103/PhysRevB.87.104109 PACS number(s): 75.50.Bb, 61.72.J−, 31.15.A−

## I. INTRODUCTION

Modern steels are multicomponent alloys that combine iron and carbon with other elements. These elements are either incorporated as impurity or added on purpose. Boron is a common additive and has a large impact on the mechanical properties of the material, although the concentration rarely exceeds a few parts per million (ppm). Apart from increased ductility,[1] tensile strength,[2,3] toughness, and creep rupture strength,[3] boron improves the hardenability of steels by retarding the austenite-to-ferrite transformation.[4] However, the maximum achievable hardenability decreases above certain boron concentrations[3,5] and fabrication temperatures, which is attributed to the formation of boron-containing phases.[6,7] Due to experimental difficulties in measuring ppm concentrations of boron and the detection limit of electron and x-ray microanalysis for light elements like boron,[8] it is not surprising that the influence of boron on mechanical properties is still discussed.[9,10]

The effect of boron on the mechanical properties is attributed to its distribution within the steel microstructure[8,11] in solid solution or in boron-containing phases or precipitates. Of particular importance are the nominal boron concentration, the fabrication process, and interactions with defects or other constituents of the steel. The latter may result in boron redistribution,[11] boride formation,[12] or redistribution of other light elements, such as carbon,[13] nitrogen,[13–15] and oxygen,[15,16] due to the formation of secondary phases.

Many of the factors that influence the distribution of boron within the steel are accessible by computational modeling. On the atomic scale, *ab initio* calculations based on density functional theory (DFT) are a well-established approach for the investigation of migration and point defects. Previous DFT studies of various light elements in α-iron addressed their solubility and migration,[17–20] their interaction with other point defects[20–25] and their effect on elastic properties.[26] However, DFT studies for boron in α-iron are rare. Only recently, Fors *et al.*[27] resolved the controversially discussed solution behavior of boron in α-iron[28–30] and identified boron as substitutional impurity with a small energy difference to the octahedral interstitial site. This substitutional solution of boron was confirmed by a subsequent DFT study of Baik *et al.*[31]

In this study, we focus on the migration of boron and its interaction with other point defects in α-iron. Section II summarizes the computational details. Section III focuses on a single boron point defect and its migration barriers and influence on elastic properties. In Sec. IV, we address the interaction of boron with other point defects and conclude our findings in Sec. V.

## II. COMPUTATIONAL DETAILS

### A. *Ab initio* calculations

The DFT calculations presented in this work used the projector augmented wave (PAW) method[32] as implemented in VASP[33] and the Perdew-Burke-Ernzerhof (PBE) functional[34] within the generalized gradient approximation (GGA) to the exchange-correlation energy. Spin-polarized calculations were used throughout the investigation. A plane-wave cutoff of 450 eV has been employed for the binary Fe-B and the ternary Fe-B-H/Al/Si/P/S system. For the ternary systems Fe-B-C/N/O, we used a plane-wave cutoff of 525 eV. Additional calculations for the validation of trends with the number of valence electrons have been performed with the same plane-wave cutoff as with the corresponding elements in the *p*-block row. Two different supercells were investigated: a $3 \times 3 \times 3$ bcc cell (54 atoms) with a $6 \times 6 \times 6$ Monkhorst-Pack *k*-point mesh[35] and a $4 \times 4 \times 4$ bcc cell (128 atoms) with a $4 \times 4 \times 4$ Monkhorst-Pack *k*-point mesh. These settings ensure that the formation energy differences are converged to within less than 1–2 meV/atom. We use the first-order Methfessel-Paxton scheme for smearing with 0.1 eV and the conjugate-gradient algorithm implemented in VASP for the relaxation of each supercell. Then we carried out one self-consistent step using

 

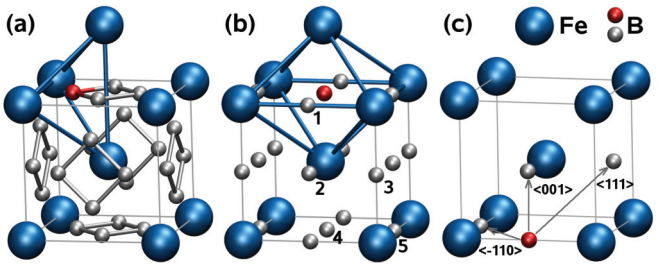


FIG. 1. (Color online) (a) Tetrahedral and (b) octahedral interstitial sites with the defect atom in red. (b) Inequivalent defect configurations are labeled by an integer number. (c) Two point defects aligned along high-symmetry axis.

the tetrahedron method with Blöchl corrections to obtain the total energy of the relaxed structure.

### B. Defect supercells

In our bcc supercell, we introduced defects either as substitutional (sub) or as interstitial atoms in the tetrahedral (tet) or octahedral (oct) site. The tetrahedral defect is positioned in the center of a distorted tetrahedron formed by four Fe host atoms [see Fig. 1(a)], with distances of either $\sqrt{3}a/2$ or $a$ between the host atoms with lattice constant $a$. The point defect has the same distance of $\sqrt{5}a/4$ to the four host atoms. The octahedral defect is in the center of a distorted octahedron formed by six Fe host atoms [see Fig. 1(b)], with distances of $\sqrt{3}a/2$ between the corner and top/bottom host atoms and a distance of $a$ between the corner host atoms, respectively. The distance between a top/bottom atom and a point defect is $a/2$, thereby smaller than the distance of $a/\sqrt{2}$ between the point defect and a corner host atom. In supercells with two point defects, both may align along high-symmetry axes [see Fig. 1(c)].

As the defects modify the equilibrium volume of the supercell, we performed calculations using two conditions; in the first set of calculations, we kept the lattice constant at our calculated value of 2.842 Å for $\alpha$-Fe (in very good agreement with experimental[36] and other theoretical values[27]) and allowed only for ionic relaxation. In the second set of calculations, we allowed for full relaxation including changes of supercell volume and shape. In either case, the interaction energy of two point defects is given as

$$E_{\mathrm{int,X+Y}} = (E_{\mathrm{Fe+X+Y}} + E_{\mathrm{Fe}}) - (E_{\mathrm{Fe+X}} + E_{\mathrm{Fe+Y}}), \quad (1)$$

where $E_{\mathrm{Fe+X+Y}}$ is the total energy of the cell including two defects. $E_{\mathrm{Fe+X}}$ and $E_{\mathrm{Fe+Y}}$ are the reference states with one defect $X$ or $Y$, and $E_{\mathrm{Fe}}$ is the reference energy of the Fe supercell. $X$ and $Y$ denote a vacancy (□) or any of the elements H, B, C, N, O, Al, Si, P, and S. $E_{\mathrm{int,X+Y}} < 0$ ($E_{\mathrm{int,X+Y}} > 0$) denotes attractive (repulsive) interaction.

### C. Migration barriers

The migration barriers were determined using the nudged elastic band (NEB) method,[37] as implemented in VASP, and refined with the climbing-image nudged elastic band (CI-NEB)[38] method if required. Due to the computational effort, we used only the $3 \times 3 \times 3$ supercell at constant volume.

TABLE I. Formation energy and differences of the formation energies (in eV) for substitutional (sub), octahedral (oct), and tetrahedral (tet) sites.

| | | B | C | N | O |
|---|---|---|---|---|---|
| $E_{\mathrm{sub}}$ | this work | 0.73 | 2.96 | 3.06 | 1.17 |
| $E_{\mathrm{oct}}$ | this work | 0.80 | 0.60 | 0.05 | −0.45 |
| $E_{\mathrm{tet}}$ | this work | 1.54 | 1.54 | 0.85 | 0.12 |
| $E_{\mathrm{sub}} - E_{\mathrm{oct}}$ | this work | −0.07 | 2.36 | 3.01 | 1.62 |
| | Ref. 27[a] | −0.06 | 2.34 | | |
| | Ref. 31[b] | −0.17 | 2.09 | | |
| $E_{\mathrm{sub}} - E_{\mathrm{tet}}$ | this work | −0.81 | 1.42 | 2.21 | 1.05 |
| | Ref. 27[a] | −0.75 | 1.49 | | |

[a]PAW, 128-atom cell, fully relaxed, PW91.
[b]FLAPW, 48-atom cell, ionic relaxation.

Further information regarding the setup of the NEB images for the different investigated migration paths are given in Sec. III.

### D. Elastic constants

For $\alpha$-Fe, we used a $1 \times 1 \times 1$ bcc cell to determine the elastic constants. Introducing one point defect in the host matrix, we used different supercell sizes (between $2 \times 2 \times 2$ and $3 \times 3 \times 4$) in order to investigate varying point defect concentrations. In all calculations, only the ions and the supercell volume were optimized prior to applying the strain tensor for calculating the elastic constants. The cell was kept cubic, as we implicitly assume that the defect atoms are randomly distributed, thus leaving the number of independent elastic constants unchanged.

## III. MIGRATION AND INFLUENCE ON ELASTIC PROPERTIES

### A. Single boron point defects

In order to determine the mechanically stable positions of boron that are possibly visited during migration, we calculated the corresponding formation energies. These are given by the difference of $\alpha$-Fe with a B defect at the sub, oct, or tet site and the total energy of Fe (B) in the corresponding $\alpha$-Fe ($\alpha$-B) ground state. The calculated formation energies for a fully relaxed $4 \times 4 \times 4$ supercell are summarized in Table I, along with corresponding formation energies for B's neighbors in the periodic table: C, N, and O. B in the substitutional site has the lowest formation energy, thus favors the replacement of an Fe host atom instead of occupying an interstitial position. This is in agreement with Refs. 27 and 31, but these works used an isolated B atom as the reference state for the calculation of the defect formation energy. Therefore we also give differences in formation energies that are independent from the reference ground state. These formation energy differences indicate consistently that at elevated temperature, B can also occupy the oct site, while the tet site is ruled out by the large energy difference.[27]

The substitutional solution of boron is different from its neighbors in the periodic table: carbon,[18] nitrogen,[21] and

oxygen[39] prefer the oct site (see Table I). The given ground-state energies were calculated with C in diamond structure and N and O as a dimer. Baik *et al.*[31] attributed the different solution behavior of B to its atomic radius, which is too large to occupy interstitial positions in $\alpha$-Fe.[40] Indeed, within the sequence B $\rightarrow$ C $\rightarrow$ N $\rightarrow$ O, the covalent radius decreases as 0.88 $\rightarrow$ 0.76 $\rightarrow$ 0.71 $\rightarrow$ 0.66 Å.[41] This leads to considerable geometric modifications in the oct case: compared to the unperturbed state, the 1NN Fe-$X$ ($X$ = B, C, N, O) distances are elongated by about 28% for B, 25% for C (in agreement with Ref. 27), 24% for N and 26–27% for O. The 2NN Fe-$X$ distances are nearly unaffected in the B case, contracted by about 2% for C and N, and elongated by about 1% for O. In the sub case, the geometrical modifications are much weaker and lead only to a few percent contraction of 1NN Fe-$X$ distances: 3–4% contraction for B, 5% for C, 4% for N, and 3% for O.

### B. Migration barriers

In our calculation of the migration barriers for substitutional and interstitial migration, we consider atomic hops to the first (1NN) or second (2NN) nearest-neighbor positions. As a dissociative (or Frank-Turnbull[42]) mechanism was proposed for the analysis of migration data,[30] we also investigated migration paths with substitutional and interstitial sites as initial and final states, respectively. We omitted the sub $\rightarrow$ $\text{oct}_{1\text{NN}}$ and sub $\rightarrow$ $\text{oct}_{2\text{NN}}$ paths as B is unstable in the oct site next to the □. We only considered the sub $\rightarrow$ $\text{oct}_{3\text{NN}}$ path, as B in the 3NN oct site remains in its site.

The atomic geometries for the five migration paths are sketched in the right panel of Fig. 2. Configurations (a) and (b) show the migration from the sub site to a 1NN vacancy along ⟨111⟩ and a 2NN vacancy along ⟨100⟩. Configurations (c) and (d) show the migration from the oct site to a 1NN oct site along ⟨100⟩ and a 2NN oct site along ⟨101⟩. Configuration (e) shows the migration path for the dissociative mechanism, where B in the sub site dissolves into B in the 3NN oct site and a vacancy. In our NEB calculations, the migration paths of substitutional and dissociative (interstitial) migration were sampled with seven (five) images. The calculated energy differences to the initial state are shown in the left panel of Fig. 2 with respect to the normalized reaction coordinate. The maximum energy along the path is identified as migration barrier $E_{\text{mig}}$. The symmetry of the migration energies reflect the identity of the initial and final state for the substitutional and interstitial mechanism [see Figs. 2(a)–2(d)]. The calculated migration barriers are summarized in Table II, along with experimental and other theoretical values for B, C, N, and O. Values in brackets have been calculated with a 4 × 4 × 4 bcc supercell for comparison, in order to quantify finite-size effects.

For B, the migration barrier for 1NN hops is in good agreement with Ref. 27 and consistently lower than the barriers for 2NN hops, i.e., 0.17 versus 1.06 eV for the substitutional mechanism and 0.70 versus 1.26 eV for the interstitial mechanism. The lowest barrier, sub $\rightarrow$ $\text{sub}_{1\text{NN}}$, requires an adjacent vacant site, thus the vacancy formation energy adds to the migration barrier for the substitutional mechanism.[27] We estimated the vacancy formation energy to 2.19 eV, similar to Ref. 27. However, we observed that an adjacent B in the 1NN (2NN) site of the vacancy reduces the

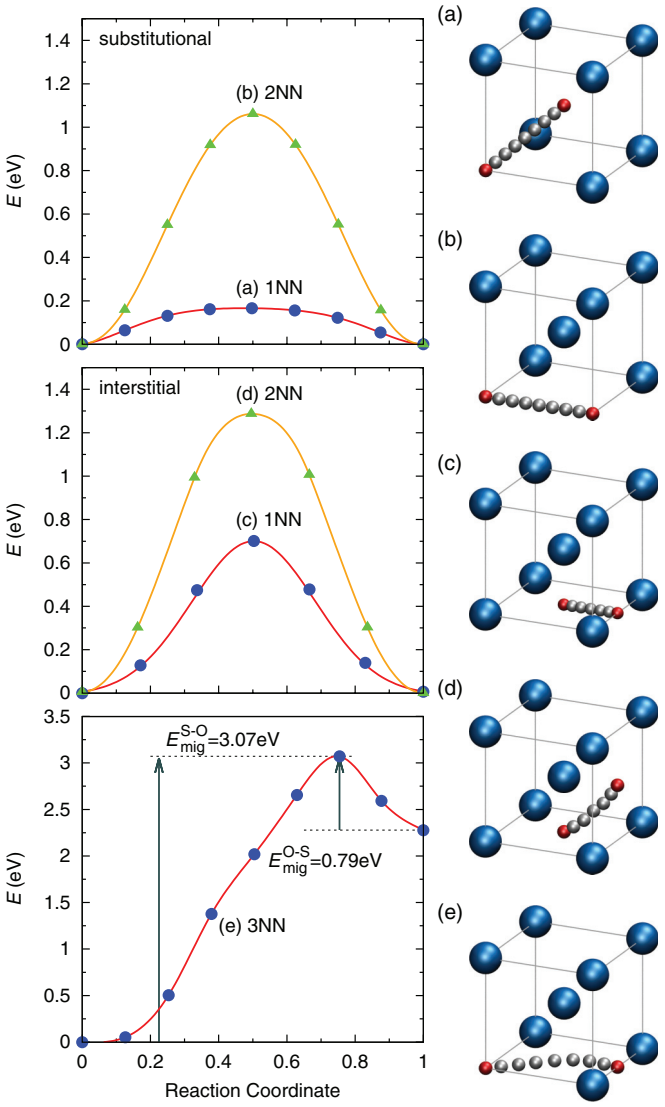


FIG. 2. (Color online) Migration path of boron for the (a) and (b) substitutional (top) and (c) and (d) interstitial (octahedral) (middle) configurations with final states in (a) and (c) first and (b) and (d) second nearest-neighbor position and the (e) dissociative mechanism (bottom) and calculated migration barriers.

vacancy formation energy to 2.09 eV (1.92 eV). This can be attributed to B-□ interactions, see Sec. III B. The inclusion of the distance-dependent vacancy formation energy increases the 1NN (2NN) migration barriers to 2.26 eV (2.98 eV). The substitutional migration is further hindered by the high barrier for vacancy diffusion of 0.55 eV (expt.),[43] close to the theoretical value of 0.65 eV.[44] These values imply that B would only jump back and forth to the vacant site, without migrating through the crystal. In contrast, the formation of a vacancy is not required for the migration of interstitial B. The calculated lowest barrier (1NN hop of 0.7 eV) is in between experimental values of 0.65 eV (see Ref. 29) and 0.92 eV (see Ref. 45) (for Fe-3%Si-B alloys). The migration barriers for the dissociative mechanism depend on the initial state: the dissociation of a B in the sub site into a B in the 3NN oct site and a vacancy requires a large energy of 3.07 eV. The opposite mechanism of an interstitial B being trapped by a vacancy requires a migration

TABLE II. Calculated migration barriers for B, C, N, and O in a $3 \times 3 \times 3$ bcc supercell. Values from Ref. 27 are listed for comparison, as well as $E_{\text{tet}} - E_{\text{oct}}$ for a $3 \times 3 \times 3$ bcc supercell at constant volume for C, N, and O among experimental and other theoretical migration barriers. Values in brackets are calculated for a $4 \times 4 \times 4$ bcc supercell with full relaxation of the cell shape and volume, in order quantify possible finite-size effects.

| Atom | Migration path | $E_{\text{mig}}$(eV) | Method |
|---|---|---|---|
| B | sub → $\text{sub}_{1\text{NN}}$ | 2.26[a] | PAW-PBE |
| | sub → $\text{sub}_{1\text{NN}}$ | 2.31[a] | PAW-PW91[b] |
| | sub → $\text{sub}_{2\text{NN}}$ | 2.98[a] | PAW-PBE |
| | oct → $\text{oct}_{1\text{NN}}$ | 0.70 (0.73) | PAW-PBE |
| | oct → $\text{oct}_{1\text{NN}}$ | 0.67 | PAW-PW91[b] |
| | | 0.65 | expt.[c] |
| | | 0.92 | expt.[d] |
| | oct → $\text{oct}_{2\text{NN}}$ | 1.26 | PAW-PBE |
| | sub → $\text{oct}_{3\text{NN}}$ | 3.07 | PAW-PBE |
| | oct → $\text{sub}_{3\text{NN}}$ | 0.79 | PAW-PBE |
| C | oct → $\text{oct}_{1\text{NN}}$ | 0.89 (0.95) | PAW-PBE |
| | oct → $\text{oct}_{1\text{NN}}$ | 0.86 | PAW-PW91[e] |
| | oct → $\text{oct}_{1\text{NN}}$ | 0.92 | USPP[f]-PW91[g] |
| | oct → $\text{oct}_{1\text{NN}}$ | 0.75 | PAW-PBE[h] |
| | | 0.81–0.87 | expt.[i] |
| N | oct → $\text{oct}_{1\text{NN}}$ | 0.72 (0.80) | PAW-PBE |
| | oct → $\text{oct}_{1\text{NN}}$ | 0.79 | USPP[f]-PW91[g] |
| | | 0.76–0.80 | expt.[j] |
| O | oct → $\text{oct}_{1\text{NN}}$ | 0.47 (0.57) | PAW-PBE |
| | | 0.93 | expt.[k] |

[a]Vacancy formation energy included.
[b]Reference 27.
[c]Reference 29.
[d]Reference 45.
[e]Reference 18.
[f]Ultrasoft pseudopotential.
[g]Reference 21
[h]Reference 46.
[i]References 43,47–49.
[j]References 47–49.
[k]Reference 50.

barrier of 0.79 eV. This value arises from the $\text{oct}_{3\text{NN}} \rightarrow \text{oct}_{2\text{NN}}$ hop, before B is dragged towards the vacancy. The deviation from the calculated oct → $\text{oct}_{1\text{NN}}$ migration barrier should be attributed to the geometric influence of the vacancy on the host Fe atoms, i.e., a slightly bent $\text{oct}_{3\text{NN}} \rightarrow \text{oct}_{2\text{NN}}$ path that circumvents the tet site. In summary, we observe relatively low migration barriers for both interstitial B and a vacancy as compared to the vacancy formation energy and the energy required to release substitutional B. As a consequence, we expect that the tendency of interstitial B to annihilate adjacent vacancies causes a reduction of the vacancy concentration and the vacancy mobility at the expense of the B mobility.

Additional calculations with a $4 \times 4 \times 4$ bcc supercell using full relaxation yielded a oct → $\text{oct}_{1\text{NN}}$ migration barrier of 0.73 eV very close to the value obtained with NEB for a $3 \times 3 \times 3$ bcc supercell with ionic relaxation only. Similar calculations for C, N, and O showed that finite-size effects influence the results by less than approximately 0.1 eV. For

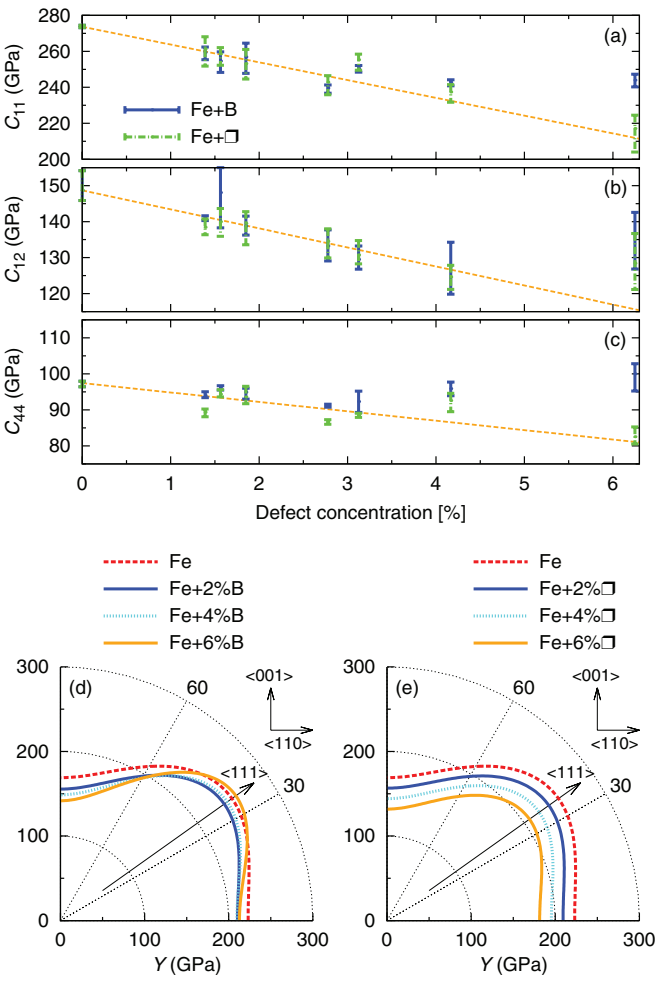


FIG. 3. (Color online) Calculated elastic constants (a) $C_{11}$, (b) $C_{12}$, and (c) $C_{44}$ for $\alpha$-Fe as a function of B and vacancy concentration. The error bars are estimated by comparing second-, third-, and fourth-order polynomials for the fit. The resulting directional dependence of the Young's modulus $Y$ is shown for (d) B and (e) □ with varying defect concentration.

C and N, the calculated values are in good agreement with previous theoretical and experimental results. For O, the calculated value agrees with a previous calculation,[39] but deviates from the experimental value, an indication that O might diffuse via a different mechanism that has not yet been considered in a theoretical investigation.

### C. Influence on Young's modulus

In order to investigate the effect of B addition on the elastic properties of $\alpha$-Fe, we determined the elastic constants of $\alpha$-Fe cells with B in the energetically favorable sub site. For comparison, we also determined the influence of a vacancy that exerts similar strain on the 1NN Fe atoms (3%–4% contraction). The computational details are described in Sec. II D.

For pure $\alpha$-Fe, we obtain $C_{11} = 274$ GPa, $C_{12} = 149$ GPa, and $C_{44} = 97$ GPa, in very good agreement to other theoretical values and with similar overestimation (underestimation) of the experimentally determined $C_{11}$ and $C_{12}$ ($C_{44}$) (c.f. Ref. 26 and references therein). Error bars for the calculated elastic

TABLE III. Linear fit for the elastic constants as a function of atomic B and □ concentration $x$. For B concentrations above 3%, we observe deviations from a simple linear relationship.

| $C_{ij}$ | <3% B | □ |
|---|---|---|
| $C_{11}(x)$ | $274-987x$ | $274-988x$ |
| $C_{12}(x)$ | $149-481x$ | $149-529x$ |
| $C_{44}(x)$ | $97-199x$ | $97-261x$ |

constants are estimated by using polynomials of different order for the fit [see Figs. 3(a)–3(c)], along with a linear fit for the calculated elastic constants as function of point defect concentration. Below a B concentration of approximately 3%, the influence of B on the elastic constants is very similar to that of a vacancy, as shown by a linear fit in Table III. Above 3% B concentration, however, the tendencies change substantially, leaving the $C_{11}$ weakly dependent on the B concentration, while $C_{12}$ and $C_{44}$ increase with B concentration. Neither volumetric nor magnetic effects could be identified as an origin of the kink in the dependence of the elastic constants on defect concentration for the case of B: the volume and magnetic moment of the supercells containing either B or □ decrease approximately linear with increasing defect concentration [see Figs. 4(a) and 4(b)] in the considered range. The impact on the volume reduction is more pronounced in the case of B. The slightly stronger reduced magnetic moment in the case of B results from the tendency of B to align its magnetic moment antiparallel to Fe. Charge density difference plots for the $3 \times 3 \times 3$ and $2 \times 2 \times 2$ supercells containing a point defect, thus representing a point defect concentration of 1.85% and 6.25%, respectively, show a virtually identical distribution of the charge density in the case of a vacancy [see Figs. 4(c) and 4(d)]. However, in the case of B, the distribution of the charge density differs in the proximity of the 2NN host Fe atom along ⟨100⟩ [see Figs. 4(e) and 4(f)]. In the $2 \times 2 \times 2$ ($3 \times 3 \times 3$) supercell, Fe and B form a Fe-B (Fe-Fe-B) chain along the ⟨100⟩ axis. Although equivalent chains are formed in the case of a vacancy, there is no notable difference in the charge density difference. Thus the influence of B on the elastic properties above a content of approximately 3% might be attributed to the formation of Fe-B chains in ⟨100⟩ or the equivalent ⟨010⟩ and ⟨001⟩ directions. However, taking into account the considered supercells, a notable impact on the elastic properties requires the formation of the Fe-B chains in at least two directions, due to twofold repetition of the single bcc unit cell in along two crystallographic axes.

We determined the directional dependence of the Young's modulus[51] for varying B [see Fig. 3(d)] and □ [see Fig. 3(e)] concentrations. For this purpose we used values of the elastic constants that were interpolated from DFT data next to the shown concentrations. For pure $\alpha$-Fe, the lowest Young's modulus is found along ⟨100⟩ with a value of $Y_{\langle 100\rangle} = 169$ GPa. The largest value is found along ⟨111⟩ with $Y_{\langle 111\rangle} = 250$ GPa. These results are in good agreement with experimental values[52,53] of $Y_{\langle 100\rangle} = 132$–$141$ GPa and $Y_{\langle 111\rangle} = 277$–$293$ GPa. Below 3% B concentration, B reduces the Young's modulus in all directions. Above 3% B concentration, we find a further reduction of the Young's modulus along the elastically soft ⟨100⟩ axis, while the elastically hard ⟨111⟩ axis

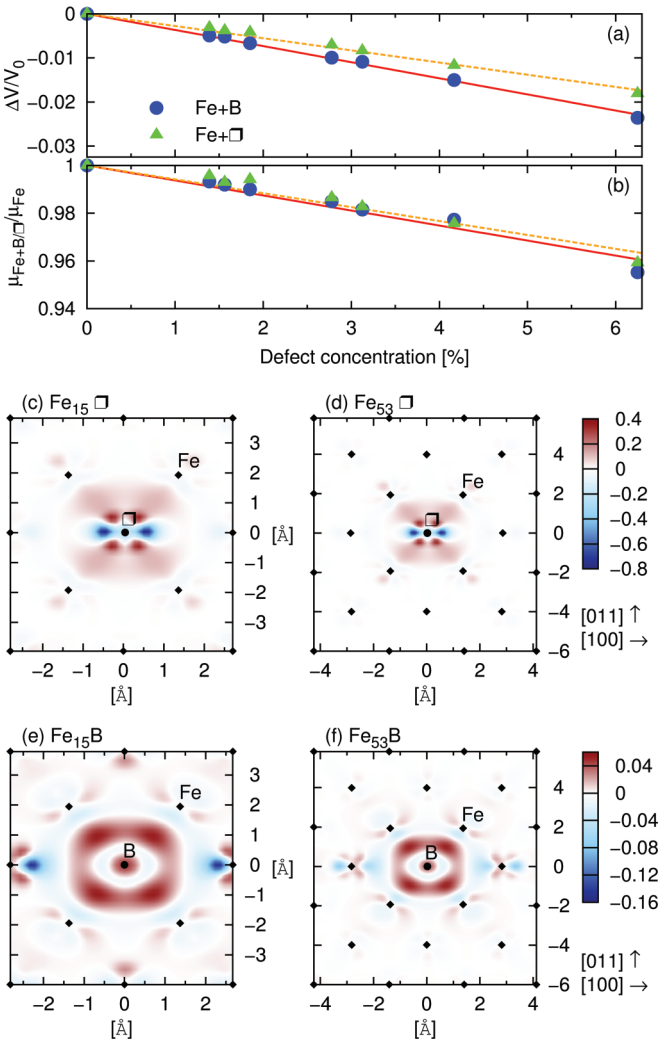


FIG. 4. (Color online) (a) Relative volume contraction and (b) reduction of normalized total magnetic moment as a function of B and □ concentrations. Charge density difference plots for the (c) and (e) $2 \times 2 \times 2$ and (d) and (f) $3 \times 3 \times 3$ supercells containing (c) and (d) a □ or (e) and (f) substitutional B.

exhibits strengthening with increasing B concentration. This corresponds to an increase of the elastic anisotropy for the case of B. In the case of a vacancy, the Young's modulus is uniformly reduced with increasing vacancy concentration.

## IV. INTERACTION WITH POINT DEFECTS

### A. Boron-boron

In the following, we characterize the interaction of two B atoms in either substitutional (sub) or interstitial octahedral (oct) site. In particular, we determined the distance-dependent interaction energy $E_{\text{int}}$ for the configurations sub-sub, sub-oct, and oct-oct (see Fig. 5). The distances that correspond to alignment along a specific crystallographic axis (c.f. Fig. 1) are indicated. All results presented in the section were obtained for $4 \times 4 \times 4$ bcc cells. We considered all inequivalent configurations of two B point defects. This leads to 13 supercells for the sub-sub case, 18 for the sub-oct case, and 31 for

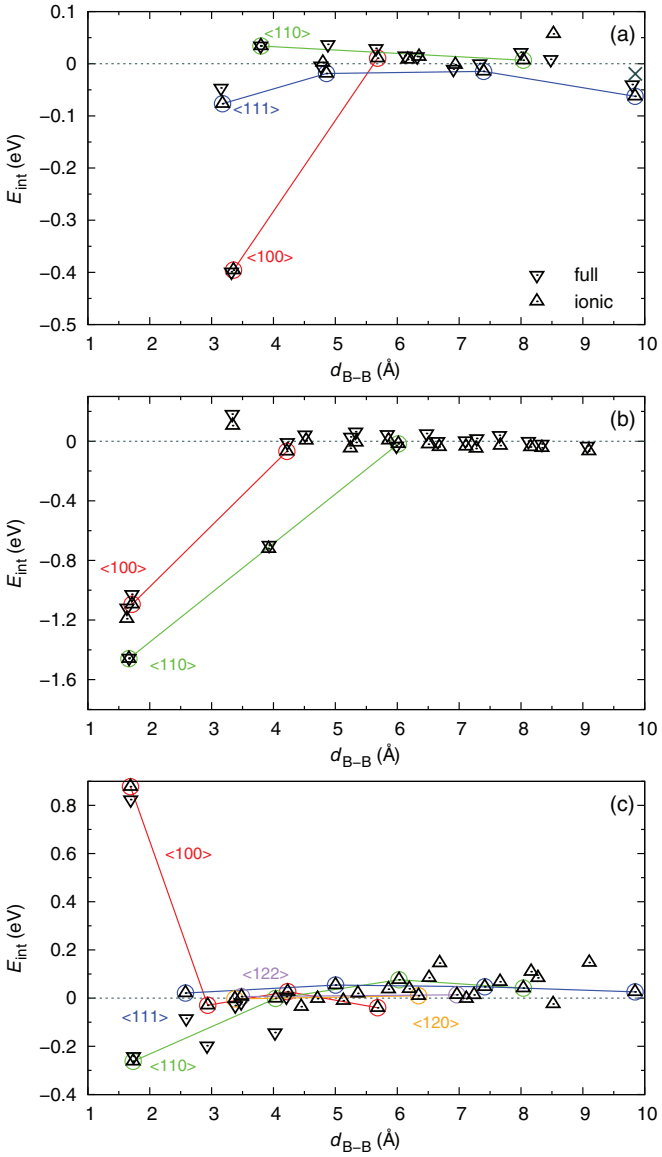


FIG. 5. (Color online) Interaction energy $E_{int}$ versus point defect distance $d_{B\text{-}B}$ for the (a) sub-sub, (b) sub-oct, and (c) oct-oct defects. High-symmetry crystallographic axes are indicated. In this and following figures, the labels "ionic" and "full" reflect the supercell relaxation: the former is performed at fixed supercell shape and volume (identical to $\alpha$-Fe) and allows only ionic relaxation, the latter allows ionic, supercell shape, and volume relaxation. The finite-size effect of nonvanishing $E_{int}$ at large $d_{B\text{-}B}$ can be reduced by breaking the symmetry as shown for a $4 \times 4 \times 5$ supercell for sub-sub [symbol $\times$ in (a)].

the oct-oct case in the $4 \times 4 \times 4$ bcc cell with varying initial defect-defect distance. For all cells, we carried out both full and ionic relaxation, unless stated otherwise.

For sub-sub [see Fig. 5(a)], the 2NN arrangement along $\langle 100 \rangle$ (the elastically soft axis) is significantly more attractive than the 1NN arrangement along $\langle 111 \rangle$ (the elastically hard axis). This behavior is virtually independent on the relaxation condition and quite different from, e.g., repulsive P-P[22] and attractive Cu-Cu[44] interactions in $\alpha$-Fe that show a monotonic decay with increasing defect-defect distance. For the 3NN arrangement along $\langle 110 \rangle$ and larger distances, the interaction energies are weak, but do not vanish in our finite-size supercell. The origin of the larger interaction energy at maximum point-defect separation is due to a highly symmetric network of B atoms. Breaking the $4 \times 4 \times 4$ symmetry by a $4 \times 4 \times 5$ supercell reduces the interaction energy [$\times$ symbol in Fig. 5(a)].

The initial 1NN, 2NN, and 4NN arrangements in the sub-oct case [see Fig. 5(b)] show large interaction energies. These are virtually independent of the relaxation condition and arise from considerable atomic relaxation of B atoms. The 1NN (2NN) configuration relaxes to a $\langle 100 \rangle$ ($\langle 110 \rangle$) dumbbell with a B-B distance of 1.71 Å (1.66 Å). Additional calculations showed that a third possible alignment along $\langle 111 \rangle$ with a shorter B-B distance of 1.63 Å is energetically in between the $\langle 110 \rangle$ and $\langle 100 \rangle$ dumbbells. Hence the observed sequence $E_{\langle 110 \rangle} < E_{\langle 111 \rangle} < E_{\langle 100 \rangle}$ of the B-B dumbbells is identical to the sequence of Fe-Fe dumbbells in $\alpha$-Fe.[54] The corresponding formation energy of the favored $\langle 110 \rangle$ alignment of 0.09 eV is significantly lower than the formation energy for substitutional and interstitial sites (c.f. Table I). Incorporation of boron complexes of up to six atoms in the vacant site yield formation energies that are above the $\langle 110 \rangle$ dumbbell. Thus the discussion whether B prefers the substitutional or octahedral site might not be relevant, as B will always bind and may primarily exist in the dumbbell configuration. The B-B distances in the dumbbells are similar to typical intericosahedra B-B bonds,[55,56] but shorter than intraicosahedral B-B bonds[57] in the $\alpha$-B and $\beta$-B polymorphs. While the 3NN configuration shows only weak repulsion, the large attractive interaction energy of the 4NN configuration arises from considerable relaxation, with B in the oct site forming a B-Fe-B complex along $\langle 111 \rangle$. The remaining configurations exhibit weak interaction energies, virtually independent of the relaxation condition.

For the oct-oct configurations [see Fig. 5(c)], we used full relaxation only for the eight shortest defect-defect distances. This choice affects only the 4NN and 7NN configurations where the octahedra surrounding both point defects have parallel alignment. We find strong repulsion for the 1NN position (along $\langle 100 \rangle$) and weak attraction for the 2NN position (along $\langle 110 \rangle$). This behavior is qualitatively different from the purely repulsive interaction of C-C, C-N, and N-N in $\alpha$-Fe.[21,25] Our DFT results of a repulsive 1NN B-B interaction using ionic and full relaxations disagree with a previous work using unrelaxed DFT calculations in combination with microscopic elasticity theory.[58] For the 4NN configuration (along $\langle 100 \rangle$), the interaction energy depends on the initial B positions: the data point shown in Fig. 5(c) corresponds to two common corner host atoms (2NN) of the octahedron [see Fig. 1(b)]. The alternative configuration with common top/bottom host 1NN atom is energetically unfavorable with $E_{int} = 1.63$ eV (1.95 eV) for calculations with full (ionic) relaxation. Simple geometry considerations might explain this large value. A single B in the oct site elongates the 1NN Fe-B distance by about 25%. This elongation is suppressed in the case of two opposing B atoms sharing the 1NN host atoms and thus lead to an energy increase. The remaining configurations, also along the $\langle 111 \rangle$, $\langle 120 \rangle$, and $\langle 122 \rangle$ crystallographic axis, show generally weak interaction energies.

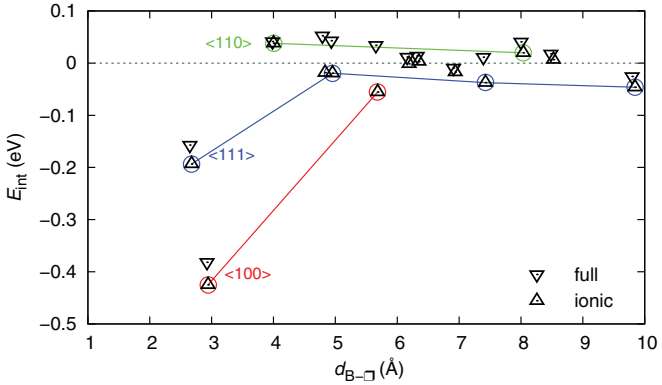


FIG. 6. (Color online) Interaction energy versus the distance between a B atom and a □. High-symmetry crystallographic axes are highlighted.

### B. Boron-vacancy

An important point-defect interaction is the boron-vacancy (B-□) interaction due to its importance for B mobility in $\alpha$-Fe.[27] The setup of our calculations was similar to B-B, except that B was restricted to occupy the sub site, as we found it to be unstable in the 1NN and 2NN oct sites relative to the vacancy. The vacancy position was taken as the geometric center of the relaxed position of the eight 1NN host atoms. The B-□ interaction (see Fig. 6) is similar to the sub-sub B-B interaction with an attractive interaction energy for the 1NN and 2NN configurations. While the interaction energy for the 1NN B-□ configuration is about three times larger than the corresponding B-B case, we find a nearly identical value for the 2NN configuration. Our calculated values are in between previous theoretical estimates of 0.091 eV (see Ref. 59) and 0.47 eV (see Ref. 60).

The attractive interaction energies might affect the mobility of substitutional B in two ways. Firstly, they increase the barrier for the vacancy migration and thereby reduce the mobility of B. Secondly, they could indicate the migration of bound B-□ complexes. Although this migration process dominates in austenitic steels[61,62] [due to a large binding energy of B-□ complexes of 0.5 eV (see Ref. 63)], no observation was reported in Fe-3%Si alloys.[64] This supports that substitutional B is rather immobile and that the interstitial mechanism is the governing migration process.

### C. Boron-hydrogen

Hydrogen is a common but unwanted impurity in steels, as it can cause embrittlement. In $\alpha$-Fe, hydrogen occupies the tet site.[17] Therefore, in order to characterize the B-H interaction, we considered the sub-tet and oct-tet defect configurations with 17 and 37 different configurations in $4 \times 4 \times 4$ supercells, respectively. Following up on our results for the B-B and B-□ interactions, we considered only the dominating shorter distances of the oct-tet configurations and additionally the maximum possible defect separation in the $4 \times 4 \times 4$ supercell. In the sub-tet case, we considered all 17 configurations.

For the sub-tet case [see Fig. 7(a)], the largest interaction energy is again found for the shortest distances. The closest

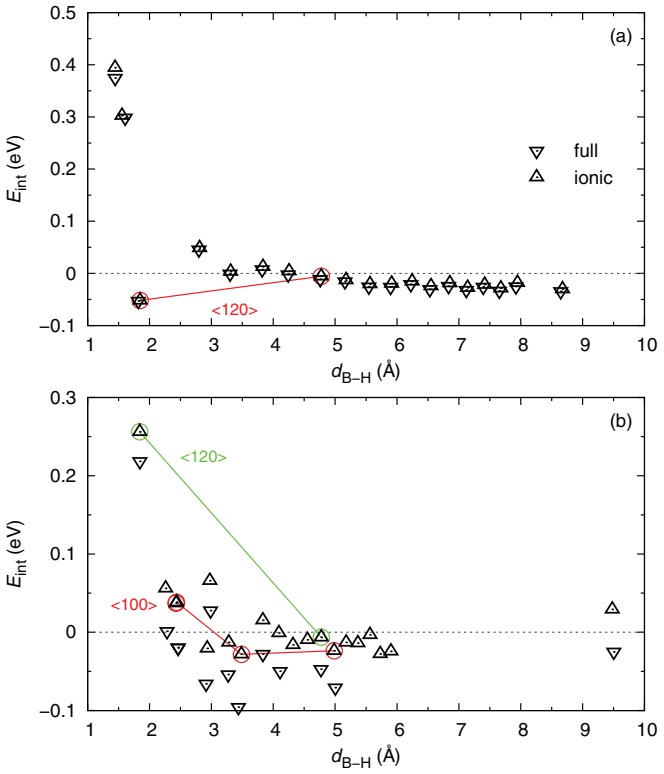


FIG. 7. (Color online) Interaction energy versus the distance between both defects for the (a) sub-tet and (b) oct-tet cases. High-symmetry crystallographic axes are highlighted.

possible arrangement of B in the sub and H in the tet site (initially along ⟨120⟩) is attractive and relaxes to a dumbbell along ⟨100⟩, similar to sub-oct for the B-B interaction. Additional calculations for dumbbells aligned along ⟨111⟩ (⟨110⟩) showed repulsive behavior with a B-H distance of 1.44 Å (1.55 Å) and $E_{int} = 0.39$ eV (0.30 eV). The initially 2NN configuration (at 2.8 Å in Fig. 7) is repulsive due to distorted local environments of both atoms that share two host Fe atoms as 1NN neighbors. The remaining configurations show weak interaction energies with a small deviation from the zero line due to finite-size effects.

For the oct-tet case [see Fig. 7(b)], the initially closest arrangement (along ⟨100⟩) is unstable and H is pushed to the nearest tet site with a weak attractive (repulsive) interaction for full (ionic) relaxation. Thus the initially second-closest arrangement becomes the mechanically stable 1NN configuration with a strong repulsive interaction energy. The interaction energies for larger distances are weakly attractive.

### D. Boron-carbon, nitrogen, oxygen

Carbon,[18] nitrogen,[21] and oxygen[39] occupy the oct site in $\alpha$-Fe, in contrast to boron. Therefore we only considered the sub-oct and oct-oct defect configurations for characterizing the B-C/N/O interactions. We further restrict ourselves to configurations with up to 7 Å (sub-oct) and 5 Å (oct-oct) distances, respectively, that we identified as typical interaction range in Secs. IV A–IV C.

The interaction energies for B-C/N/O sub-oct configurations are shown in Fig. 8(a), including also the B-B case for

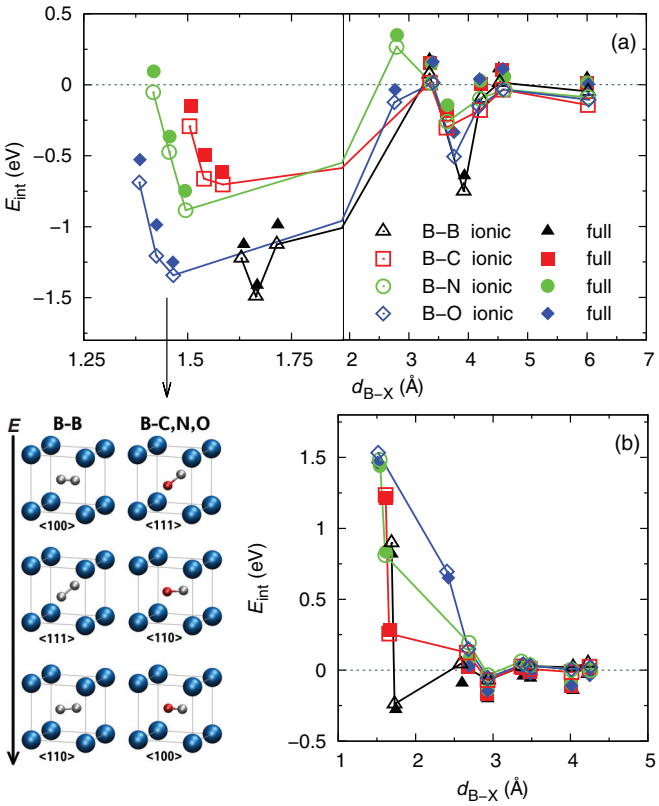


FIG. 8. (Color online) Interaction energy versus the distance between defects for (a) sub-oct and (b) oct-oct configurations, including the B-C, B-N, and B-O cases. The results for B-B (see Fig. 5) are also shown for direct comparison. In the sub-oct case, configurations with a defect-defect distance below 2 Å represent dumbbell configurations. A finer scale of the abscissa was used in this range. The corresponding sequence of stability is sketched in the bottom left of the figure.

comparison, recalculated with the same $E_{cut}$. We observe the same tendency of interaction energies for all types of second defect with the largest magnitude for B-B, followed by B-O, and weaker magnitude for B-C and B-N. Similar to the B-B interaction, the 1NN (2NN) configuration of B-C forms a ⟨100⟩ (⟨110⟩) dumbbell. However, in the B-N and B-O cases, only the 1NN configuration forms a ⟨100⟩ dumbbell, while the 2NN is repulsive. Additional calculations showed that B-C, B-N, and B-O favor the ⟨100⟩ dumbbell, followed by the ⟨110⟩ and ⟨111⟩ dumbbells (see Table IV). This is in contrast to B-B with the stability sequence ⟨110⟩, ⟨111⟩, and ⟨100⟩. The distances between the point defects within the dumbbells generally match typical bond lengths in bulk phases: the B-C dumbbell bond lengths of 1.50–1.58 Å lie in between typical B-C bond lengths found in the only carbide listed in the experimental phase diagram,[65] hR45-$B_{13}C_2$,[66] and agree well with tabulated B-C bond lengths in organic compounds.[67,68] The only boron nitride listed in the experimental phase diagram,[69] hR6-BN,[70] with a B-N bond length of 1.446 Å, as well as tabulated values,[68] are close to our findings of 1.42–1.50 Å in the B-N dumbbells. The B-O distances of 1.38–1.47 Å for the dumbbells are longer than the bond length reported in Ref. 67, but match the tabulated values in Ref. 68. In the 4NN configuration of sub-oct B-B, the two B atoms form a B-Fe-B chain along ⟨111⟩ with a large $E_{int}$. In the B-C, B-N, and B-O cases, however, the oct atoms remain in their position, although we obtain large interaction energies. This effect might be due to favorable geometrical alignment with one of the host Fe atoms as 1NN to both, B in the sub and C/N/O in the oct sites: substitutional B tends to contract 1NN Fe-B distances, while octahedral C/N/O tends to elongate the 1NN Fe-$X$ distance, hence giving rise to the attractive interaction energy. Consistently, we find the strongest geometric modifications for the largest influence on the interaction energy in the case of B-O. This tendency of B to bind to point defects was also confirmed experimentally[71] for C and O.

In extension to our calculations of dumbbell interaction energies, we further investigated the B-N and B-O cases where we had to force the formation of a ⟨110⟩ dumbbell. This indicates the existence of an additional barrier for the formation of the ⟨110⟩ dumbbell, which does not exist for B-B and B-C. In order to estimate the height of the barrier and to explain this behavior, we performed a CI-NEB calculation. For both the B-N and B-O cases, we used the distant alignment with B (N,O) in the sub (oct) site as an initial state and the forced, close alignment (i.e., the ⟨110⟩ dumbbell) as a final state. The energy versus defect-defect distance, as calculated with seven NEB images, is shown in Fig. 9 (some images represented virtually identical energies and defect-defect distances, but differing reaction coordinates, thus not all seven images are visible in Fig. 9). The plot shows clearly the existence of the barrier for dumbbell formation in B-N and B-O with migration barriers of $E_{mig}^{B\text{-}N} = 0.40$ eV and $E_{mig}^{B\text{-}O} = 0.23$ eV, respectively.

The energies for the oct-oct interaction are shown in Fig. 8(b), also including the B-B interaction for comparison. The 1NN configurations exhibit the same repulsive behavior of the interaction energy with increasing magnitude going from B over C to N and O. The same tendency of increasing interaction energy is observed for the 2NN configurations, with a transition of attractive to repulsive interaction energy in going from B to C, and a different defect-defect distance for B-O. The trend of increasing interaction energies with the number

TABLE IV. Interaction energies in eV of the dumbbell alignments for supercells with full and only ionic relaxation. The relaxation condition alters the interaction energy in the range 0.1–0.2 eV, but does not affect the stability sequence of the dumbbells.

| | B-B | | B-C | | B-N | | B-O | |
|---|---|---|---|---|---|---|---|---|
| | full | ionic | full | ionic | full | ionic | full | ionic |
| ⟨100⟩ | −0.99 | −1.12 | −0.62 | −0.70 | −0.75 | −0.88 | −1.25 | −1.34 |
| ⟨110⟩ | −1.41 | −1.49 | −0.50 | −0.66 | −0.36 | −0.47 | −0.99 | −1.21 |
| ⟨111⟩ | −1.12 | −1.22 | −0.15 | −0.30 | 0.10 | −0.05 | −0.53 | −0.69 |

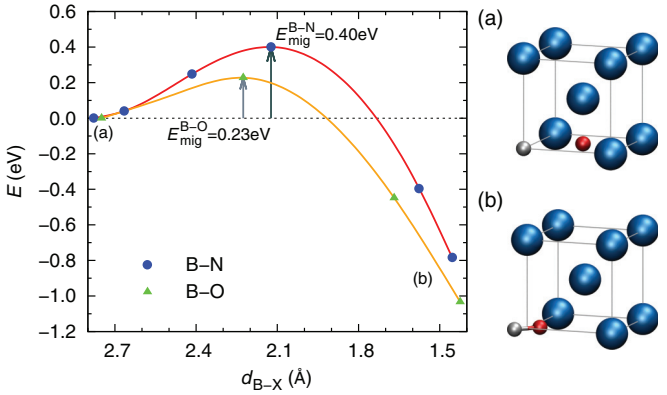


FIG. 9. (Color online) Energy versus defect-defect distance for B-N and B-O. The initial state (a), both point defects in their site, and final state (b), representing the dumbbell, are sketched in the right panel. The existence of the barrier results from a compression of the B-N and B-O bonds, respectively. The barrier is higher for B-N with $E^{B-N}_{mig} = 0.40$ eV than for B-O with $E^{B-O}_{mig} = 0.23$ eV.

of valence electrons of the point defects has also been observed in Refs. 25 and 58. For the unfavorable 4NN configuration (c.f. Sec. IV A), we find 1.55 eV (1.95 eV) for C with full (ionic) relaxation, 1.50 eV (1.90 eV) for N and 1.46 eV (1.85 eV) for O [not shown in Fig. 8(b)]. As in the case of B-B (c.f. Sec. IV A), the reduced interaction energies for full relaxation is due to the volume expansion of the supercells that increases the distance between point defects and the common 1NN Fe host atom.

### E. Boron-aluminum, silicon, phosphorus, sulfur

Experimental and theoretical investigations showed Al,[72] Si,[20,73] and P[22] to favor the sub site in $\alpha$-Fe. Sulfur is also referred to as substitutional element in $\alpha$-Fe.[24] This is in line with our calculated formation energy differences of $E_{sub} - E_{oct} = -2.18$ eV and $E_{sub} - E_{tet} = -2.25$ eV ($3 \times 3 \times 3$ supercell, ionic relaxation). Therefore we only considered the sub-sub and sub-oct configurations, with B in either the sub or oct site.

The interaction energies for sub-sub are shown in Fig. 10(a). The interaction of B with Si and P resembles the B-B and B-□ interactions with a larger magnitude for the 2NN arrangement than for the 1NN. For Al, the interaction is attractive (weakly repulsive) for the 1NN (2NN) arrangement. For S, both the 1NN and 2NN arrangements yield an attractive interaction of similar strength. The overall attractive interaction of B in the sub site with point defects described in Secs. IV A–IV D is also observed for the second-row elements Al, Si, P, and S. The difference of full and only ionic relaxation for the interaction energies is negligible. The dip in the interaction energy for the 5NN arrangement can be associated to matching strain effects with B and the second point defect aligned along ⟨111⟩ with a host Fe atom in between: Al/Si/P/S tends to decrease the distance towards the shared Fe host atom in contrast to B. The strongest effect is found for Al, the largest considered second-row *p*-block element, and decreases with decreasing atomic size.

For B in the oct site [see Fig. 10(b)], the 1NN and 2NN arrangements yield repulsive (attractive) interactions for Al,

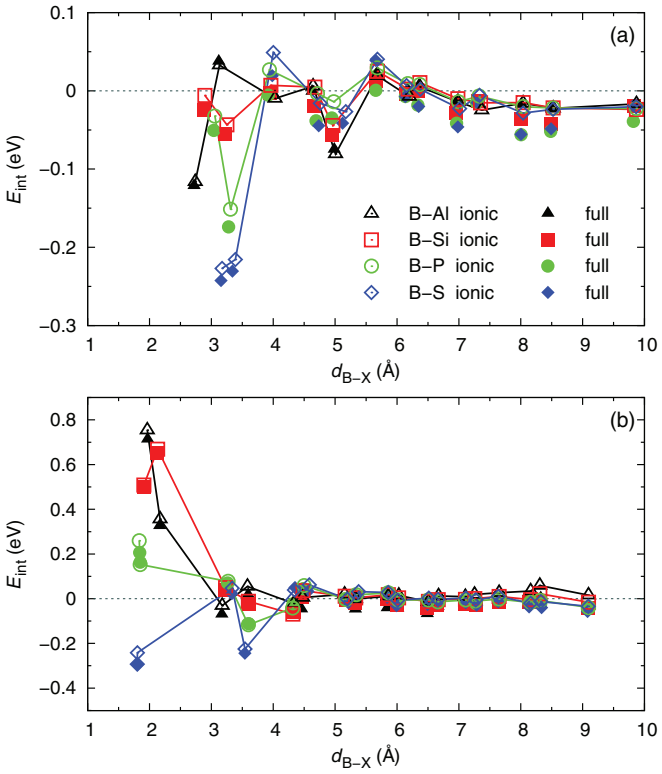


FIG. 10. (Color online) Interaction energy versus the distance between defects for (a) sub-sub and (b) oct-sub configurations for B-Al/Si/P/S.

Si, and P (S). The interaction energies for 1NN and 2NN B-S for only ionic and fully relaxed supercells are similar and overlap in Fig. 10(b). In the case of Al and Si, both point defects remain in their respective initial sub and oct sites, while P and S show dumbbell formation. This tendency has also been found for close sub-oct (sub-tet) configurations for B-B/C/N/O (B-H) (c.f. Secs. IV A, IV C, and IV D). However, the solely repulsive interaction of B-P deviates from the attractive interaction in the aforementioned configurations, while S-B matches the tendency. For both B-P and B-S, the most favorite alignment is along ⟨100⟩, followed by ⟨110⟩. For completeness, we also calculated the ⟨111⟩ alignment, with interaction energies of $E_{int} = 0.60$ eV (0.67 eV) for P with full (ionic) relaxation and $E_{int} = 0.30$ eV (0.37 eV) for S [not shown in Fig. 10(b)]. Thus the stability sequence of dumbbells for B-P/S matches the sequence for B-H/C/N/O dumbbells. The dip in the 4NN arrangement has also been observed in the sub-oct configurations for B-B/C/N/O and is attributed to matching strain effects. Here, the interaction varies with atomic size, being weakest for the largest element Al, and increases form Si to P and S with decreasing atomic size.

### F. Discussion

#### *1. Trends with band filling*

The considered point defects B, C, N, and O, as well as Al, Si, P and S, are in the same row of the periodic table. Therefore we discuss the calculated interaction energies also in terms of filling the *p* orbitals with an increasing number of valence electrons (see Fig. 11). For completeness, we add results for

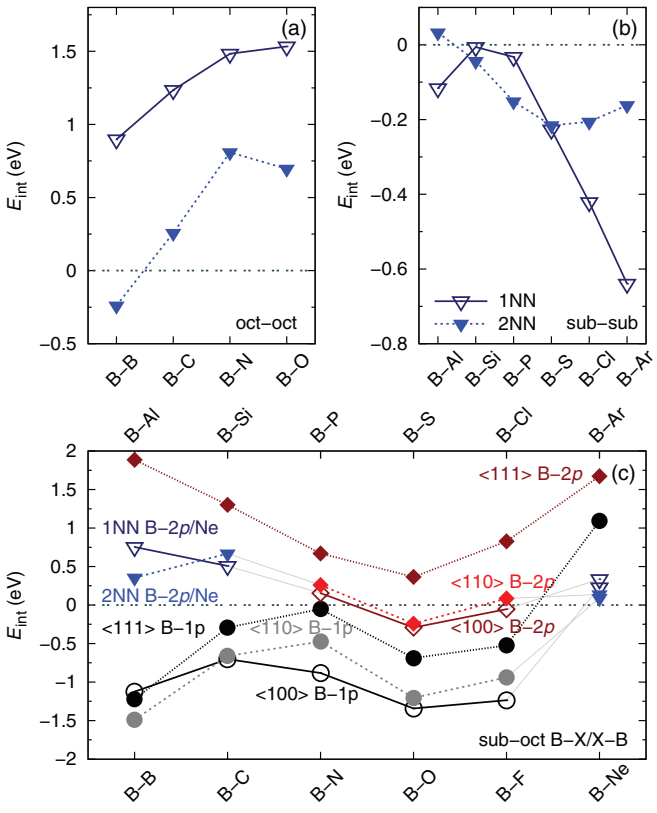


FIG. 11. (Color online) Interaction energies of supercells with ionic relaxation for the (a) 1NN/2NN oct-oct and (b) sub-sub configurations and the (c) dumbbell and 1NN/2NN sub-oct configurations (○ $1p$ dumbbell, ◇ $2p$ dumbbell, ▽ no dumbbell).

the elements F, Ne, Cl, and Ar, which are substitutional defects in $\alpha$-Fe (see Table V). For Cl and Ar, this is in line with the other second-row $p$-block elements. F and Ne, on the contrary, deviate from their direct neighbors in the first row, but match B. We restrict the considered configurations to the three dumbbells in the sub-oct case and the 1NN/2NN sub-oct/oct-oct/sub-sub configurations. All other configurations with weaker interactions are not considered in the following discussion in trends with band filling. However, we exclude solely interstitial configurations containing F and Ne due to their substitutional solution and significantly larger formation energy difference to the interstitial sites, as compared to B. We further restrict the discussion to supercells with only ionic relaxation.

For oct-oct B-B/C/N/O [see Fig. 11(a)], the interaction energy for the 1NN arrangement increases with the band filling of the second point defect. The interaction energy for the 2NN arrangement increases monotonically from B-B to B-N. B-O deviates from this tendency due to the significantly larger point defect separation compared to the other cases [c.f. Fig. 8(b)]. For sub-sub B-Al/Si/P/S/Cl/Ar [see Fig. 11(b)], only the interactions for B-Si and B-P are in line with the tendency of a larger interaction energy for the 2NN arrangement observed for B-B and B-□. B-Al has the same number of valence electrons as B-B, but differs significantly in the interaction energy with an attractive (repulsive) interaction for the 1NN (2NN) arrangement. The trends for the 1NN and 2NN arrangements of B-Al/Si/P/S with band filling are in line with □-Al/Si/P/S interactions:[74] a parabolic behavior for 1NN and monotonically decreasing behavior for the 2NN configuration.

For mixed configurations, i.e., point defects in the sub and oct sites [see Fig. 11(c)], all investigated $p$-block elements showed dumbbell formation, except B-Al/Si/Ar/Ne. In these four cases, the point defects remain in their respective defect sites. The interaction energies of the dumbbells along ⟨100⟩, ⟨110⟩, and ⟨111⟩ for B-B/C/N/O/F (marked as ○) follow a parabola with band filling centered on C and N. The kink in the tendency for B-F and B-Ne is due to the switched point defect sites for the reference states, Fe/Ne in the sub and B in the oct site. The trend in the interaction energy of the dumbbells for B-P/S/Cl (marked as ◇) is similar to the isovalent systems B-N/O/F. However, the energies are shifted upwards. This shift appears also in the other isovalent system without formation of ⟨100⟩ and ⟨110⟩ dumbbells (marked as ▽, alignment along ⟨111⟩ is forced). For B-Al/Ne/Ar, the 2NN arrangement has lower interaction energy than the 1NN arrangement.

TABLE V. Formation energy difference (in eV) between substitutional and interstitial point defects F, Ne, Cl, and Ar in $\alpha$-Fe ($3 \times 3 \times 3$ supercell, ionic relaxation).

| | F | Ne | Cl | Ar |
|---|---|---|---|---|
| $E_{sub} - E_{oct}$ | −0.77 | −3.41 | −2.29 | −3.78 |
| $E_{sub} - E_{tet}$ | −1.03 | −3.31 | −2.30 | −3.64 |

### 2. *Role of atomic size*

The formation of dumbbells observed in the majority of considered systems raises the question which factors drive their formation and their stability sequence. The most intuitive factor for dumbbell formation is the atomic size of the point defect atoms. Tabulated covalent radii[41] for the $p$-block elements decrease monotonically with increasing number of valence electrons, except for the noble gases Ne and Ar, with the second-row $p$-block elements having larger covalent radii. Therefore we determined the effective radius $r_{eff}$ of isolated, substitutional point defects as half the distance to the 1NN host Fe atoms. The sub site is not the favored defect site for H, C, N, and O, but the dumbbells represent a substitutional defect. Contrary to the tabulated covalent radii, both rows in the $p$-block show a parabolic-like dependence of the effective radius on the number of valence electrons, with the center shifted to less valence electrons for the first row (see Fig. 12). We note that the atomic size correlates well with the interaction energies for the second row [c.f. Fig. 11(c)]. Despite the small covalent radius of H, its effective radius is comparable to the first-row $p$-block elements. We find that the dumbbell-forming elements have a smaller effective radius than bulk $\alpha$-Fe. The elements, that do not show dumbbell formation, Al/Si/Ne/Ar, have an effective radius that is similar or larger than the effective radius of bulk $\alpha$-Fe. The only exception from this general trend is Cl that shows weakly bound dumbbells for an effective radius that is slightly larger than Fe. This finding indicates that the occurrence of dumbbell formation might be determined by the atomic size of the point defects. Comparisons of B-N/P, B-O/S, and B-F/Cl show that

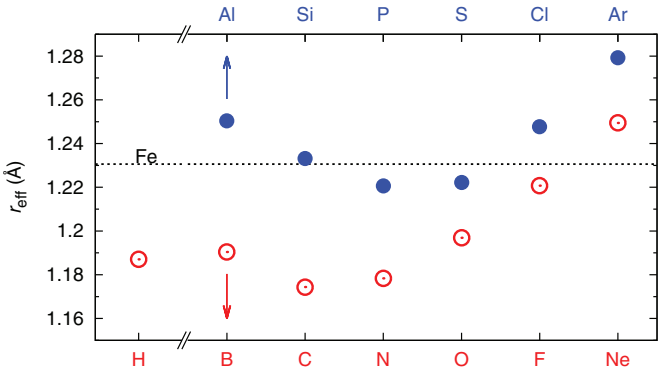


FIG. 12. (Color online) Calculated effective radii for point defects in $\alpha$-Fe.

an isovalent decrease of effective radii leads to more stable dumbbells. This dependence is inverted for comparisons of interstitial elements within the first $p$-block row.

### 3. *Stability sequence of single-type dumbbells*

The stability sequence ⟨110⟩, ⟨111⟩, ⟨100⟩ of B-B dumbbells is identical to the sequence of Fe-Fe dumbbells in $\alpha$-Fe,[54] but differs from the sequence ⟨100⟩, ⟨110⟩, ⟨111⟩ of all other B-containing dumbbells. The former sequence is not solely related to dumbbells formed by point defects of the same type, as corresponding calculations for C-C and N-N (see Table VI) show that these dumbbells also favor the latter sequence.

References 21, 24, and 25 investigated the stability of oct-□-oct complexes containing interstitial C and N. We note that complexes aligned along ⟨100⟩ and ⟨110⟩ containing interstitial B are not stable, and the B atoms relax towards the dumbbell configuration. We observed a similar trend for single interstitial B atoms in 1NN or 2NN position with respect to a vacancy. A oct-□-oct complex with ⟨111⟩ alignment is not possible in bcc. For C, dumbbell formation is favored over the oct-□-oct complex. This is inverted for N. For O, only the ⟨111⟩ dumbbell appears. Along ⟨100⟩, the oct-□-oct is the only configuration that is mechanically stable. Along ⟨110⟩, we observe a configuration that is neither a dumbbell nor an oct-□-oct complex with an interaction energy of $E_{\text{int}} = -2.07$ eV that is in between the ⟨100⟩ oct-□-oct complex and the ⟨111⟩ dumbbell.

### 4. *Mechanical and chemical contribution*

For further analysis of the interaction between the point defects, we decompose the interaction energy into a chemical and a mechanical contribution that quantifies the lattice distortion due to dumbbell formation. Such a decomposition

TABLE VI. Interaction energies (in eV) for single-type dumbbells and oct-□-oct complexes.

| | dumbbell | | | oct-□-oct | |
|---|---|---|---|---|---|
| atom | ⟨100⟩ | ⟨110⟩ | ⟨111⟩ | ⟨100⟩ | ⟨110⟩ |
| C-C | −1.66 | −1.65 | −1.19 | −1.32 | −0.36 |
| N-N | −0.22 | 0.34 | 1.29 | −1.96 | −0.74 |
| O-O | . . . | . . . | −0.89 | −3.54 | . . . |

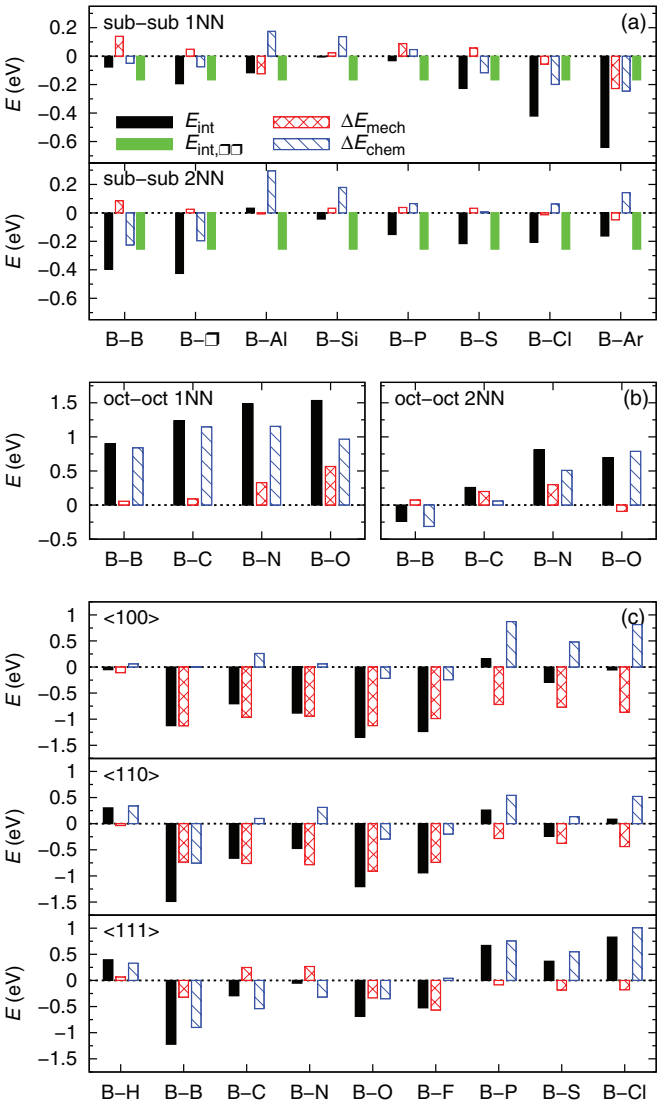


FIG. 13. (Color online) Decomposition of interaction energy in mechanical, chemical, and optional □-□ interaction energies for (a) sub-sub, (b) sub-oct, and (c) dumbbell-forming sub-oct/tet configurations.

has been successfully applied to the solution energy of B and C in bulk $\alpha$-Fe by Fors *et al.*[27] Here, we extend this approach to the decomposition of defect interaction energies. By expressing $E_{\text{int}}$ in terms of formation energies, we can rewrite Eq. (1) as

$$E_{\text{int,X+Y}} = \Delta E_{\text{mech}} + \Delta E_{\text{chem}}, \tag{2}$$

where $\Delta E_{\text{mech}}$ and $\Delta E_{\text{chem}}$ are the differences of mechanical and chemical energies between supercells with point defects $X + Y$ and with point defect $X$ and $Y$. This is valid for all oct-oct and sub-oct configurations, if in the latter case, one of the point defects occupies the sub site. For sub-sub configurations, however, the □-□ interaction energy $E_{\text{int},\square\square}$ enters as an additional term, and Eq. (2) becomes

$$E_{\text{int,X+Y}} = E_{\text{int},\square\square} + \Delta E_{\text{mech}} + \Delta E_{\text{chem}}. \tag{3}$$

Our calculated value of $E_{\text{int},\square\square} = -0.17$ eV (−0.26 eV) for the 1NN (2NN) arrangement is in good agreement with

previous DFT calculations.[24] The larger magnitude in $E_{\text{int}}$ for the 2NN arrangement is in line with B-B/□/Si/P. For B-B/□, the attractive interaction in the 1NN (2NN) arrangement is mainly attributed to $E_{\text{int},\square\square}$ ($E_{\text{int},\square\square}$ and $\Delta E_{\text{chem}}$), while $\Delta E_{\text{mech}}$ is repulsive [see Fig. 13(a)]. For 1NN arrangements with second-row $p$-block elements, the trends in $E_{\text{int}}$ can be decomposed into a monotonically decreasing $\Delta E_{\text{chem}}$, parabolic-like $\Delta E_{\text{mech}}$, that correlates inversely with the atomic size (c.f. Fig. 12), and a constant $E_{\text{int},\square\square}$. $\Delta E_{\text{mech}}$ is significantly weaker for the 2NN arrangement, and the change in the trend of $E_{\text{int}}$ for late second-row elements is to a large degree determined by $\Delta E_{\text{chem}}$. For oct-oct configurations [see Fig. 13(b)], the trends in $E_{\text{int}}$ correlate well with $\Delta E_{\text{mech}}$, but not with $\Delta E_{\text{chem}}$. We note that the deviating trend for B-O is solely attributed to $\Delta E_{\text{mech}}$, which is in line with the significantly increased point defect separation [c.f. Fig. 8(b)]. For the dumbbell-forming sub-oct/tet configurations [see Fig. 13(c)], we find that the mechanical contribution yields throughout the stability sequence ⟨100⟩, ⟨110⟩, ⟨111⟩. This sequence can be attributed to an increasing asymmetry in the host lattice distortion required for dumbbell incorporation and corresponds to the stability sequence governed by $E_{\text{int}}$ for all configurations except B-B. We further note that $\Delta E_{\text{mech}}$ generally represents a significant attractive contribution in $E_{\text{int}}$ for ⟨100⟩ and ⟨110⟩ dumbbells. The sequence of the chemical contribution, however, does not correlate with the alignment, but depends on the constituent dumbbell atoms and varies even among isovalent systems. For the ⟨100⟩ and ⟨110⟩ dumbbells, the trends in the chemical contribution correlate well with $E_{\text{int}}$, except for the ⟨111⟩ dumbbell. For B-B, the altered stability sequence can be attributed to the negligible chemical contribution of the ⟨100⟩ dumbbell, compared to the other two alignments, that shifts this alignment upwards. This makes the ⟨110⟩ dumbbell the favorite one.

## V. CONCLUSIONS

In this work, we present extensive density functional theory calculations of B point defects in $\alpha$-Fe. In particular, we determined the migration barriers, the influence on elastic properties, and the interaction of B atoms with other point defects, in particular, a vacancy, H, B, C, N, O, Al, Si, P, and S. In order to discuss trends with band filling, we also included F, Ne, Cl, and Ar.

(1) The migration barriers for 1NN hops of a single B point defect as obtained with the NEB method are in good agreement with previous results. Taking into account also 2NN hops in the NEB calculations, our calculations show that 1NN hops are preferred over 2NN hops for both substitutional and interstitial migrations. Including the vacancy formation energy as an additional barrier for substitutional migration, the sequence changes to 1NN/2NN interstitial, 1NN/2NN substitutional, despite a reduction of the vacancy formation energy in the presence of a B atom. B atoms that diffuse via an interstitial mechanism are likely to be trapped by vacancies, and the energy required for release of B from the vacancy (3.07 eV) exceeds the vacancy formation energy.

(2) In order to understand the direction dependence of the B point defect interactions, we also determined the influence of B on the elastic properties of $\alpha$-Fe. Below a B concentration of approximately 3%, the impact of B on the elastic constants and Young's modulus, with the largest (weakest) relative change along the elastically soft (hard) axis, is virtually identical to the influence of a vacancy. Above a B content of approximately 3%, $C_{12}$ and $C_{44}$ increase, while $C_{11}$ remains approximately constant with increasing B content. This leads to an increased anisotropy of the Young's modulus.

(3) Introducing a second point defect, we calculated the interaction energy with B atoms as a function of separation. In particular, we considered a second substitutional and octahedral B atom, a vacancy, tetrahedral H atom, octahedral C, N, and O atoms, and substitutional Al, Si, P, and S atoms. Substitutional F, Ne, Cl, and Ar atoms were additionally investigated to discuss trends with band filling. We find a general tendency that substitutional B tends to bind point defects, while interstitial B tends to repel them. Trends in the interaction of substitutional B resemble interactions of vacancies with point defects. Interstitial B behaves similar to interstitial C and N.

(4) For small separation between substitutional and interstitial point defects, we observed dumbbell formation in all configurations except B-Al/Si/Ne/Ar. We can attribute this finding to the size of the dumbbell atoms. Furthermore, we find the ⟨110⟩ dumbbell to be favored by B-B, and the ⟨100⟩ dumbbell to be favored by all other configurations. The stability sequence of dumbbell alignments can be explained by the mechanical distortions to the Fe host matrix. The only exception is the ⟨100⟩ B-B dumbbell that is less stable than the ⟨110⟩ and ⟨111⟩ dumbbells due to a negligible chemical contribution.

## ACKNOWLEDGMENTS

We gratefully acknowledge fruitful discussions with E. R. Margine and A. N. Kolmogorov and financial support through ThyssenKrupp AG, Bayer MaterialScience AG, Salzgitter Mannesmann Forschung GmbH, Robert Bosch GmbH, Benteler Stahl/Rohr GmbH, Bayer Technology Services GmbH, and the state of North-Rhine Westphalia as well as the EU in the framework of the ERDF.

[1] S. I. Bulat, N. A. Sorokina, and E. A. Ulyanin, Met. Sci. Heat Treat. **17**, 712 (1975).
[2] J. A. Jiménez, G. González-Doncel, and O. A. Ruano, Adv. Mater. **7**, 130 (1995).
[3] P. N. Ernst, P. J. Uggowitzer, and M. O. Speidel, J. Mater. Sci. Lett. **5**, 835 (1986).
[4] L. Lanier, G. Metauer, and M. Moukassi, Mikrochim. Acta **114-115**, 353 (1994).
[5] A. A. Azarkevich, L. V. Kovalenko, and V. M. Krasnopolskii, Met. Sci. Heat Treat. **37**, 22 (1995).
[6] S. Watanabe and H. Ohtani, Trans. ISIJ **23**, 38 (1983).
[7] S. Watanabe, H. Ohtani, and T. Kunitake, Trans. ISIJ **23**, 120 (1983).

[8]J. Lis, A. Lis, and C. Kolan, Metalurgija **50**, 123 (2011).
[9]R. K. Guseinov, Met. Sci. Heat Treat. **36**, 544 (1994).
[10]W. Stumpf and K. Banks, Mater. Sci. Eng. A **418**, 86 (2006).
[11]X. L. He and Y. Y. Chu, J. Phys. D: Appl. Phys. **16**, 1145 (1983).
[12]A. N. Kolmogorov, S. Shah, E. R. Margine, A. F. Bialon, T. Hammerschmidt, and R. Drautz, Phys. Rev. Lett. **105**, 217003 (2010).
[13]B. S. Seong, Y. R. Cho, E. J. Shin, S. I. Kim, S.-H. Choi, H. R. Kim, and Y. J. Kim, J. Appl. Cryst. **41**, 906 (2008).
[14]L. H. Chown and L. A. Cornish, Mater. Sci. Eng. A **494**, 263 (2008).
[15]Z. Adolf, J. Bažan, and L. Socha, Mater. Technol. **45**, 111 (2011).
[16]N. Valle, J. Drillet, A. Pic, and H.-N. Migeon, Surf. Interface Anal. **43**, 753 (2011).
[17]D. E. Jiang and E. A. Carter, Phys. Rev. B **70**, 064102 (2004).
[18]D. E. Jiang and E. A. Carter, Phys. Rev. B **67**, 214103 (2003).
[19]C.-C. Fu and F. Willaime, Phys. Rev. B **72**, 064117 (2005).
[20]D. Simonovic, C. K. Ande, A. I. Duff, F. Syahputra, and M. H. F. Sluiter, Phys. Rev. B **81**, 054116 (2010).
[21]C. Domain, C. S. Becquart, and J. Foct, Phys. Rev. B **69**, 144112 (2004).
[22]C. Domain and C. S. Becquart, Phys. Rev. B **71**, 214109 (2005).
[23]C.-C. Fu, E. Meslin, A. Barbu, F. Willaime, and V. Oison, Solid State Phenom. **139**, 157 (2008).
[24]T. Ohnuma, N. Soneda, and M. Iwasawa, Acta Mater. **57**, 5947 (2009).
[25]Y. You, M. F. Chan, and H. T. Chen, Comp. Mater. Sci. **67**, 222 (2013).
[26]D. Psiachos, T. Hammerschmidt, and R. Drautz, Acta Mater. **59**, 4255 (2011).
[27]D. H. R. Fors and G. Wahnström, Phys. Rev. B **77**, 132102 (2008).
[28]P. E. Busby and C. Wells, J. Met. **6**, 972 (1954).
[29]W. R. Thomas and G. M. Leak, Nature (London) **176**, 29 (1955).
[30]Y. Hayashi and T. Sugeno, Acta Metall. **18**, 693 (1970).
[31]S. S. Baik, B. I. Min, S. K. Kwon, and Y. M. Koo, Phys. Rev. B **81**, 144101 (2010).
[32]P. E. Blöchl, Phys. Rev. B **50**, 17953 (1994).
[33]G. Kresse and J. Hafner, Phys. Rev. B **47**, 558 (1993); G. Kresse and J. Furthmüller, *ibid*. **54**, 11169 (1996).
[34]J. P. Perdew, K. Burke, and M. Ernzerhof, Phys. Rev. Lett. **77**, 3865 (1996).
[35]J. D. Pack and H. J. Monkhorst, Phys. Rev. B **13**, 5188 (1976); **16**, 1748 (1977).
[36]I. Seki and K. Nagata, ISIJ Int. **45**, 1789 (2005).
[37]H. Jónsson, G. Mills, and K. W. Jacobsen, in *Classical and Quantum Dynamics in Condensed Phase Simulations*, edited by B. J. Berne, G. Ciccotti, and D. F. Coker (World Scientific, Singapore, 1998), Chap. 16, p. 385.
[38]G. Henkelman, B. P. Uberuaga, and H. Jónsson, J. Chem. Phys. **113**, 9901 (2000).
[39]A. Janotti and C. L. Fu, APS March Meeting Abstracts, S16.004 (2003).
[40]V. N. Voyevodin, I. M. Neklyudov, V. V. Bryk, and O. V. Borodin, J. Nucl. Mater. **271-272**, 290 (1999).
[41]B. Cordero, V. Gómez, A. E. Platero-Prats, M. Revés, J. Echeverría, E. Cremades, F. Barragán, and S. Alvarez, Dalton Trans. **21**, 2832 (2008).
[42]F. C. Frank and D. Turnbull, Phys. Rev. **104**, 617 (1956).
[43]S. Takaki, J. Fuss, H. Kugler, U. Dedek, and H. Schultz, Rad. Eff. **79**, 87 (1983).
[44]C. Domain and C. S. Becquart, Phys. Rev. B **65**, 024103 (2001).
[45]W. Wang, S. Zhang, and X. He, Acta Metall. Mater. **43**, 1693 (1995).
[46]M. Kabir, T. T. Lau, X. Lin, S. Yip, and K. J. Van Vliet, Phys. Rev. B **82**, 134112 (2010).
[47]T. Hejnal, Czech. J. Phys. B **29**, 1149 (1979).
[48]M. Mondino and A. Seeger, Scr. Metall. **11**, 817 (1977).
[49]J. R. G. da Silva and R. B. McLellan, Mater. Sci. Eng. **26**, 83 (1976).
[50]J. Takada and M. Adachi, J. Mater. Sci. **21**, 2133 (1986).
[51]M. A. Hopcroft, W. D. Nix, and T. W. Kenny, J. Microelectromech. **19**, 229 (2010).
[52]J. Prohászka and J. Dobránszky, Mater. Sci. Forum **414-415**, 311 (2003).
[53]J. J. Adams, D. S. Agosta, R. G. Leisure, and H. Ledbetter, J. Appl. Phys. **100**, 113530 (2006).
[54]C.-C. Fu, F. Willaime, and P. Ordejón, Phys. Rev. Lett. **92**, 175503 (2004).
[55]M. Widom and M. Mihalkovič, Phys. Rev. B **77**, 064113 (2008).
[56]J. L. Hoard, D. B. Sullenger, C. H. L. Kennard, and R. E. Hughes, J. Solid State Chem. **1**, 268 (1970).
[57]A. Masago, K. Shirai, and H. Katayama-Yoshida, Phys. Rev. B **73**, 104102 (2006).
[58]A. Udyansky, J. von Pezold, A. Dick, and J. Neugebauer, Phys. Rev. B **83**, 184112 (2011).
[59]S. Zhang, X. He, and T. Ko, J. Mater. Sci. **29**, 5549 (1994).
[60]S.-H. Song, R. G. Faulkner, and P. E. J. Flewitt, J. Mater. Sci. **34**, 5549 (1999).
[61]L. Karlsson, H. Norden, and H. Odelius, Acta Metall. **36**, 1 (1988).
[62]D. J. Mun, E. J. Shin, and Y. M. Koo, Nucl. Eng. Technol. **43**, 1 (2011).
[63]R. G. Faulkner, J. Mater. Sci. **16**, 373 (1981).
[64]S. Zhang, X. He, Y. Chu, and T. Ko, J. Mater. Sci. **29**, 2633 (1994).
[65]L. Kaufman, B. Uhrenius, D. Birnie, and K. Taylor, Calphad **8**, 25 (1984).
[66]A. Kirfel, A. Gupta, and G. Will, Acta Cryst. B **35**, 1052 (1979).
[67]A. Gupta, A. Kirfel, G. Will, and G. Wulff, Acta Cryst. B **33**, 637 (1977).
[68]F. H. Allen, O. Kennard, D. G. Watson, L. Brammer, A. G. Orpen, and R. Taylor, J. Chem. Soc. Perkin Trans. II **12**, S1 (1987).
[69]H. Okamoto, J. Phase Equilib. **21**, 208 (2000).
[70]V. L. Solozhenko, G. Will, H. Hüpen, and F. Elf, Solid State Commun. **90**, 65 (1994).
[71]G. Dubben, M. N. Chandrasekharaiah, and B. H. Kolster, J. Mater. Sci. **27**, 3192 (1992).
[72]A. Taylor and R. M. Jones, J. Phys. Chem. Solids **6**, 16 (1958).
[73]M. Polcarová, K. Godwod, J. Bak-Misiuk, S. Kadečková, and J. Brádler, Phys. Stat. Sol. A **106**, 17 (1988).
[74]O. I. Gorbatov, P. A. Korzhavyi, A. V. Ruban, B. Johansson, and Yu.N. Gornostyrev, J. Nucl. Mater. **419**, 248 (2011).